



Estimating $ZZ \rightarrow ll\nu\nu$ background in the $ll + E_T^{miss}$ final state using $Z\gamma \rightarrow ll\gamma$ data

A Thesis

submitted to

Indian Institute of Science Education and Research, Pune
in partial fulfillment of the requirements for the
BS-MS Dual Degree Programme

by

Mangesh Sonawane

Registration Number: 20121083



Indian Institute of Science Education and Research, Pune
Dr. Homi Bhabha Road,
Pashan, Pune 411008, INDIA

June 2017 - April 2018

Conducted at : DESY
Notkestraße 85,
22607, Hamburg
Germany

Supervisor: Dr. Beate Heinemann
©Mangesh Sonawane 2018
All rights reserved

Certificate

This is to certify that this dissertation, entitled "Estimating $ZZ \rightarrow ll\nu\nu$ background in the $ll + E_T^{miss}$ final status using $Z\gamma \rightarrow ll\gamma$ data", submitted towards the partial fulfilment of the BS-MS dual degree programme at the Indian Institute of Science Education and Research (IISER), Pune, represents the work carried out by Mangesh Sonawane at the Deutsches Elektronen-Synchrotron (DESY), Hamburg, under the supervision of Dr. Beate Heinemann, Professor of Experimental Particle Physics at the Institute of Physics, University of Freiburg, during the academic year 2017-2018.

Mangesh Sonawane

Dr. Beate Heinemann

Committee:

Dr. Beate Heinemann

Dr. Seema Sharma

I dedicate this thesis to my parents, Avinash and Ranjana Sonawane, my mentors, Dr. Sourabh Dube and Dr. Seema Sharma, and to my friends and colleagues and IISER, without whose timely advice and support this thesis would not have been made possible.

Declaration

I hereby declare that the matter contained within the thesis entitled "Estimating $ZZ \rightarrow ll\nu\nu$ background in the $ll + E_T^{miss}$ final state using $Z\gamma \rightarrow ll\gamma$ data", contains the results of the work carried out by me at the Deutsches Elektronen-Synchrotron (DESY) Hamburg, under the supervision of Dr. Beate Heinemann, and the same has not been submitted elsewhere for any other degree.

Mangesh Sonawane

Dr. Beate Heinemann

Committee:

Dr. Beate Heinemann

Dr. Seema Sharma

Acknowledgements

I would like to express my deepest gratitude for Dr. Beate Heinemann for her guidance and patient mentoring. It's not just technical skills that I have acquired under her supervision, but also an understanding of how a physicist approaches the subject and tackles the inevitable problems that surface.

⟨ placeholder ⟩

Abstract

In the search for Dark Matter (DM) at the LHC, SM particles are produced in association with DM particles, which are invisible as they don't interact with the detector. Thus events with large imbalance in transverse momentum are of interest. One such signature is $l\bar{l} + E_T^{miss}$. The dominant background contributing to the search for DM in the $l\bar{l} + E_T^{miss}$ is $ZZ \rightarrow l\bar{l}\nu\nu$. Currently, this background is determined using Monte Carlo simulation, with an uncertainty of $\approx 10\%$ [22]. The goal of this study is to establish a data driven method to estimate this background, and reduce the uncertainty. Using $Z\gamma \rightarrow l\bar{l}\gamma$, which is a process with low backgrounds and has a high $BR \times \sigma$, it is possible to estimate the $ZZ \rightarrow l\bar{l}\nu\nu$ contribution. In regions where $p_T(\gamma) \gg M_Z$, the two processes are kinematically similar. They have the same production mechanisms, but differ due to the photon and Z boson couplings to the quarks being different, as well as the difference in mass (photons are massless, while Z bosons are massive). Introducing a transfer factor R as the ratio $\sigma(ZZ)/\sigma(Z\gamma)$ which is determined from simulation, the contribution of $ZZ \rightarrow l\bar{l}\nu\nu$ to the background can be estimated from $Z\gamma \rightarrow l\bar{l}\gamma$ data. The uncertainty on the prediction of R due to theoretical aspects is estimated in this work.

Contents

Abstract	i
1 Introduction	1
1.1 The Standard Model	2
1.2 Inadequacies of the Standard Model	4
1.2.1 Beyond the Standard Model	4
1.2.2 Dark Matter	5
2 The Large Hadron Collider	7
3 Theoretical Aspects	9
3.1 Invisible Higgs in association with a Z boson - ZH	9
3.2 Background estimation: ZZ	10
3.3 Transfer factor R	11
3.4 Theoretical Uncertainties	12
3.5 Approach	12
4 Theoretical uncertainties on cross sections and the transfer factor R	13
4.1 MCFM	13
4.2 Results	14
4.2.1 Uncertainty from Scale Variation	17
4.2.2 Uncertainty from PDF variation	20
4.2.3 Uncertainty from Photon Fragmentation	21
5 Additional Figures	23

Chapter 1

Introduction

The Standard Model of physics is one of the most successful theories developed, describing the fundamental particles and their interactions [1]. It is theoretically self-consistent, and has enjoyed tremendous success in providing accurate experimental predictions. However, the Standard Model is not complete theory of fundamental interactions. It does not provide an explanation for several observed phenomena, such as gravity, or the accelerating expansion of the universe, among others.

One such question that triggers burning curiosity is the apparent incongruity of galaxy rotation curves with the theory of Newtonian mechanics: stars in the arms of spiral galaxies appear to move much faster than Newtonian physics would predict. Either the current understanding of mechanics is incomplete, or there is more mass present somewhere in the galaxy that is not visible by any method that is currently employed. This invisible hunk of matter is what is termed as Dark Matter (DM).

Detailed observations of these rotation curves, along with measurements of other phenomena such as gravitational lensing by distant galaxies, galaxy clusters, and Cosmic Microwave Background (CMB) lead to the conclusion that, if the Dark Matter hypothesis is true, the amount of visible Baryonic matter in the universe is a mere 4%. The remaining 96% of the universe is composed of Dark Matter and Dark Energy.

Now it becomes important to address the question: what exactly is Dark Matter?

Several extensions to the Standard Model, called Beyond Standard Model (BSM) theories, attempt to provide an explanation of these observed phenomena. Dark Matter hasn't been observed to interact directly through the electromagnetic force, and are thus invisible to current detectors. Consequently candidates for Dark Matter are called Weakly Interacting Massive Particles (WIMPs). In LHC experiments, events with WIMPs in the final state show up as an imbalance in the momentum in the plane transverse to the beam (referred to as E_T^{miss} throughout this thesis).

One such BSM theory postulates that these Dark Matter candidate particles may couple to Standard Model particles in interactions mediated by the Higgs boson. Fig 1.1 illustrates some of the possible processes for the production of the Higgs boson. The Higgs boson can then decay into invisible particles.



Figure 1.1: Feynman diagrams for the Standard Model production of the Higgs boson; VH: Higgs produced in association with a W/Z boson (top left), ggF: gluon-gluon fusion (top right), VBF: vector boson fusion (bottom left), ttH: (bottom right). The Higgs boson then further decays into invisible DM particles.

In this thesis, a closer look is taken at the VH channel, in particular ZH , where the Higgs boson decays invisibly into DM particles, and the Z boson decays into a dilepton pair. The signature of such a process is $ll + E_T^{miss}$. A possible search in this channel would constitute stacking all known Standard Model processes that contribute to the $ll + E_T^{miss}$ signal (making up the background) and look for excesses in data which will indicate the presence of non-Standard-Model processes. In this thesis, a closer look is taken at the $ZZ \rightarrow ll\nu\nu$ process, which constitutes the dominant SM background in the $ll + E_T^{miss}$ final state. However, it is difficult to discriminate between the Standard Model $ZZ \rightarrow ll\nu\nu$ and $ZH \rightarrow l^+l^- + E_T^{miss}$, the process under consideration, because of the identical final state. Thus, an attempt is made to estimate it using alternate processes with clean signals.

1.1 The Standard Model

The Standard Model is the name given to the theory of particles, fundamental forces, and interactions that govern the Universe. It describes three of the four forces: the electromagnetic, strong and weak forces. Figure 1.2 shows a schematic representation of the elementary particles in the Standard Model.

The Standard Model classifies fundamental particles as either Fermions or Bosons:

- **Fermions:** make up the matter in the universe. Fermions are spin 1/2 particles, and are categorized into quarks and leptons. Quarks exist in 6 flavors, up, down, charmed, strange, top (or truth) and bottom (or beauty). Leptons too exist in 6 flavors: electrons, muons, and taus, and their respective neutrinos. The up, charmed and top quarks carry an electric charge of $+2/3e$. The down, strange and bottom quarks carry an electric charge of $-1/3e$. The electron, muon and tau carry an electric charge of $-1e$, and the neutrinos carry no electromagnetic charge. Here, e is the unit of electromagnetic charge, and is equal to 1.602×10^{-19} Coulombs. Quarks and leptons are divided into three generations, with each generation having more mass than the last. Each fermion has a parity inverted counterpart, called an anti-particle, having the same mass, but an opposite charge. For example, an anti-electron (or a positron) has a charge of $+1e$ and a down anti-quark will have charge of $+1/3e$.
- **Bosons:** are particles with integral spin that mediate the interactions between particles in the universe. There are four gauge bosons: the photon, which mediates electromagnetic interactions, the W and Z bosons that mediate weak interactions, and the gluons, which mediate strong interactions. These are vector bosons, having spin $+1$. In addition, there is a scalar boson (spin 0), the Higgs boson, which gives particles their mass.

Standard Model of Elementary Particles

three generations of matter (fermions)				
	I	II	III	
mass	$\approx 2.4 \text{ MeV}/c^2$	$\approx 1.275 \text{ GeV}/c^2$	$\approx 172.44 \text{ GeV}/c^2$	0
charge	$2/3$	$2/3$	$2/3$	0
spin	$1/2$	$1/2$	$1/2$	1
QUARKS	u up	c charm	t top	g gluon
	d down	s strange	b bottom	γ photon
	e electron	μ muon	τ tau	Z Z boson
LEPTONS	ν_e electron neutrino	ν_μ muon neutrino	ν_τ tau neutrino	W W boson
				H Higgs
				SCALAR BOSONS
				GAUGE BOSONS

Figure 1.2: A schematic representation of the Standard Model [2] of particles. The table shows the three generations of fermions (classified as quarks and leptons) that are the building blocks of all known matter in the Universe, and bosons that mediate interactions, and are thus responsible for 'forces'

The Standard Model addresses three of the four fundamental forces; it does not address the Gravitational force. The strong, weak and electromagnetic forces can be described by the $SU(3) \times SU(2) \times U(1)$ local gauge symmetry group, where the $SU(3)$ symmetry group describes the strong interaction, and the electroweak interactions are based on the $SU(2) \times U(1)$ symmetry group. There are $8+3+1$ generators associated with this model, each generator corresponding to a vector boson.

Thus, there are 8 gluons, which are massless spin 1 particles with an intrinsic property called color charge, that mediate strong interactions (described by Quantum Chromodynamics). They are responsible for interactions between quarks (leptons do not interact via the strong force) as quarks have a non vanishing color charge. At low energies, quarks cannot be found in isolation, instead occurring in triplets called *Baryons*, such as protons, or a bound quark-antiquark pair, called *Mesons*. This is because of color confinement [3].

The interaction of the scalar Higgs field with the vector fields W^+ , W^- , W^0 and B causes the spontaneous breaking of the $SU(2) \times U(1)$ symmetry, resulting in 3 massive and one massless gauge boson. It also implies the existence of a neutral scalar boson, known as the Higgs boson, which was discovered in July 2012 [4]. The generators of $SU(2) \times U(1)$ correspond to the W^+ , W^- and Z bosons, massive vector bosons (spin 1) that mediate weak interactions, and the massless vector boson γ (photon), which mediates electromagnetic interactions. The W bosons are charged, whereas the Z boson and γ are neutral.

1.2 Inadequacies of the Standard Model

Despite its immense success, the Standard Model does not paint a complete picture of everything that we observe. It does not account for several phenomena that are experimentally observed, such as:

- Gravity: The Standard Model does not include gravity. If, analogous to the other forces, a 'graviton' is introduced into the Standard Model as an extension, it does not describe what is observed experimentally. In fact, the Standard Model is incompatible with general relativity [5].
- Dark Matter and Dark Energy: Cosmological observations, such as galaxy rotation curves, do not match predictions based on the visible amount of mass in the universe. A fit with the observations predicts additional invisible matter, called Dark Matter [6]. Similarly, the universe is expanding at an accelerating rate, which hints at the existence of Dark Energy [7]. The Standard Model does not account for exotic matter such as these. In fact, the Standard Model only accounts for about 4% of the content of the universe [8, 9].
- Neutrino masses: Neutrinos are assumed to be massless in the Standard Model. However, neutrino oscillations have recently been observed [10], which is only possible if neutrinos have mass [11].
- Matter-antimatter asymmetry: According to the Standard Model, matter and antimatter should be created in equal quantities. However, the universe appears to have a preference for matter, indicating that in its initial state of the universe, this symmetry was broken [12].
- Hierarchy problem [13–16]: Quantum corrections to the Higgs mass are divergent, and force it to be very large. However, experiments show a surprisingly small number for the Higgs mass, at 125 GeV. There appear to be some extraordinary fine tuned cancellations that make this mass so small.

The Standard Model is incomplete, and thus requires modifications or additions to it, which are collectively called Beyond Standard Model (BSM) theories.

1.2.1 Beyond the Standard Model

Several extensions to the Standard Model have been proposed that attempt to address some of its inadequacies.

Supersymmetry (SUSY) attempts to reconcile gravity with the SM, and adds another symmetry to the Standard Model, predicting the existence of *supersymmetric* partners, called sparticles, to Standard Model particles. For example, sleptons are supersymmetric partners to the corresponding leptons, and differ by spin 1/2. SUSY would also resolve the hierarchy problem by ensuring that the divergences would cancel out at all orders in the perturbation expansions, if the superpartners have mass near the electroweak scale (broadly, between 100 and 1000 GeV).

The observation of neutrino oscillations imply that neutrinos have mass, however, these observations can only reveal the mass difference between the different neutrino flavors. The absolute mass of the neutrinos has been constrained to have an upper limit of 2 eV, much smaller than the lightest SM particles, by precision measurements of tritium decays. To incorporate neutrino masses, an extension to the Standard Model, the see-saw mechanism, introduces right handed neutrinos and couples them to left-handed neutrinos with a Dirac mass term.

Both SUSY and the addition of a sterile right-handed neutrino to the SM are extensions that provide candidates for Dark Matter. These candidates are known as Weakly Interacting Massive Particles (WIMPs). They do not interact electromagnetically, and are thus invisible to most detectors.

1.2.2 Dark Matter

Cosmological observations of galaxies made over the decades, such as the velocity curves of galaxies (called galaxy rotation curves) indicate an anomaly; the stars in the arms of spiral galaxies appear to move faster than what would be expected from Keplerian relations, using the visible mass from the galaxies. Figure 1.3 shows the two rotation curves, expected and observed, of NGC 6503, a field¹ spiral galaxy. [17]

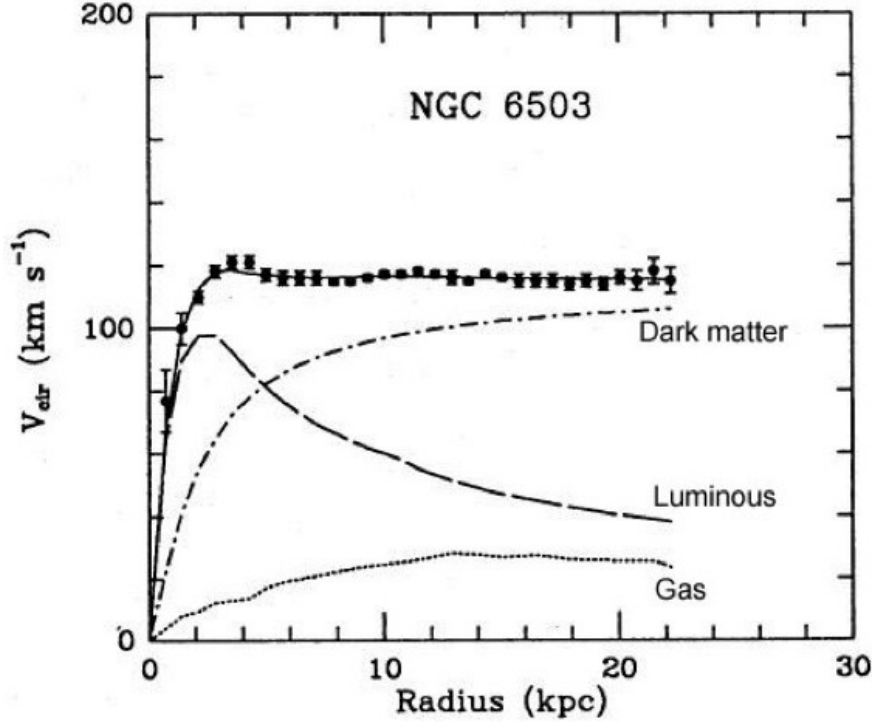


Figure 1.3: Velocity of stars in NGC 6503, a field spiral galaxy, as a function of radial distance from the center of the galaxy [17]. The 'Luminous' curve is what would be expected from the visible mass, but what is observed is much higher, indicating excess invisible matter.

Either the current understanding of Newtonian Mechanics is incomplete, or there is additional mass that is not visible which is contributing to the mass term in Newton's equation. This invisible mass is what is termed as Dark Matter. Ergo, Dark Matter appears to interact gravitationally, but not electromagnetically, with visible (Standard Model) matter. It is possible that Dark Matter is made up of an exotic and hitherto undiscovered kind of matter, and searches are underway at the LHC to look for Dark Matter via its interactions with the Standard Model.

There is additional cosmological evidence supporting Dark Matter, such as gravitational lensing of distant galaxies, structure formation in the early universe, anisotropy in the cosmic microwave background, etc.

Dark Matter searches at the Large Hadron Collider

As Dark Matter does not interact electromagnetically, any Dark Matter particles produced in collider experiments will be invisible to detectors at the LHC. Thus, in event reconstruction, such events are expected to be marked by a significant imbalance in transverse momentum (E_T^{miss}). Currently, Dark Matter searches are conducted at the LHC [18]. Dark Matter particles are denoted by χ .

¹Field galaxies do not belong to a large cluster, and are thus gravitationally isolated

- Mono χ searches : These searches look for the production of a Standard Model particle in association with E_T^{miss} . Figure 1.4 shows the Feynman diagrams for the Mono-X processes.
 - Mono-jet : In theory, it is possible to produce Dark Matter particles in association with one or more QCD jets from initial state radiation. Thus mono-jet searches look for one or more jets in events with large E_T^{miss} .
 - Mono-V : In a similar manner to mono-jet searches, a mono-V search looks for a single vector (γ, W or Z) boson. If DM particles couple directly to a pair of gauge bosons, this may be the dominant mode of DM production.
 - Mono-Higgs : It may also be that a single Higgs boson is produced in association with E_T^{miss} . Such events would be characterised by a $H \rightarrow \gamma\gamma$ or $H \rightarrow b\bar{b}$ final state.

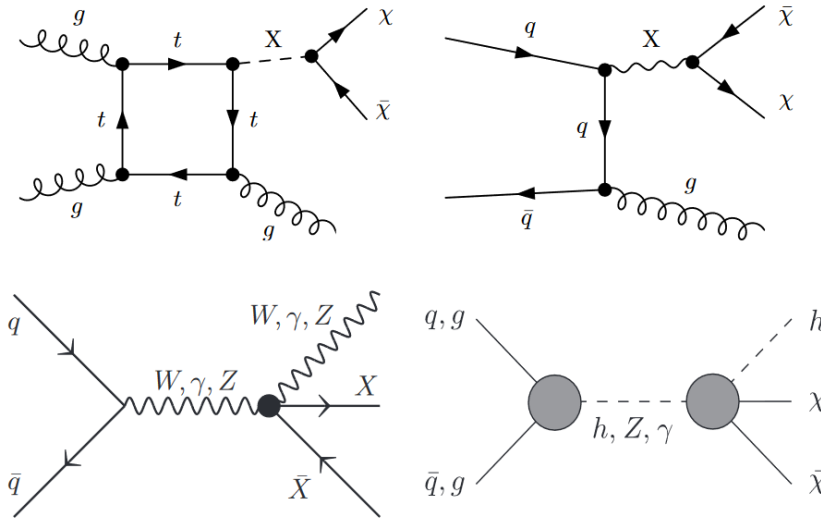


Figure 1.4: Feynman diagrams for mono X processes, showing mono-jet production (top) induced by gluons (top left) and quarks (top right) [19] where the mediator X can be a scalar, pseudo-scalar, vector or axial-vector particle; mono-V (bottom left) [20]; and mono-higgs (bottom right) [21], where h is the Standard Model Higgs boson with mass 125 GeV.

- DM+top : If DM particles couple predominantly to heavy quark flavors, a search for a top quark pair is a promising direction to head in.
- Invisible Higgs : If the mass of the DM particles is less than half the mass of the Higgs boson, it may be possible that the DM particles couple to the Standard Model via the Higgs boson, i.e $H \rightarrow \chi\chi$ processes. The main methods of Standard Model Higgs production are shown in Figure 1.1.
 - Vector boson fusion (VBF): In VBF processes, the Higgs is produced from the interaction of two vector bosons.
 - Production of Higgs in association with a massive vector boson (VH) : This mechanism, together with VBF are the most important methods of Higgs production in invisible Higgs searches. Such events can be recognised with a large imbalance in transverse momentum, as well as the decay products of the vector boson.
 - Gluon gluon fusion (ggF) : It is also possible for the Higgs to be produced from the interaction of gluons.

This thesis investigates the Standard Model background to the $ll + E_T^{miss}$ signal with respect to the production of an invisible Higgs in association with a leptonically decaying gauge boson. Chapter 2 gives an overview of the Large Hadron Collider, the ATLAS detector, and details the event topology. Chapter 3 address the theoretical framework of this thesis.

Chapter 2

The Large Hadron Collider

Chapter 3

Theoretical Aspects

3.1 Invisible Higgs in association with a Z boson - ZH

In this thesis, the production of the Higgs boson, in association with a Z boson is considered. In this model, as shown in Figure 3.1, the Higgs boson mediates the interaction between Dark Matter particles and Standard Model particles, and the Z boson decays into a lepton-antilepton pair. As Dark Matter is invisible to current detectors, this process results in the $ll + E_T^{miss}$ signature. The main Standard

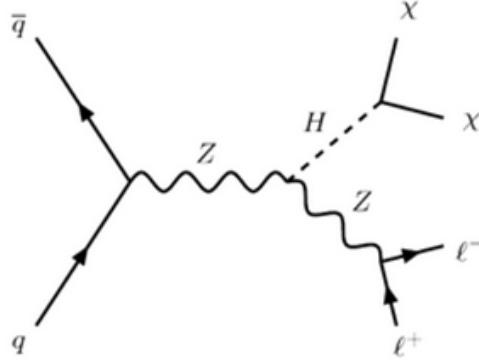


Figure 3.1: Feynman diagram showing the associated production of a Higgs boson with a Z boson. The Higgs boson decays to two invisible DM particles and the Z boson decays leptonically, resulting in the $ll + E_T^{miss}$ signature.

Model background processes for the $ll + E_T^{miss}$ final state are $ZZ \rightarrow ll\nu\nu$, $WZ \rightarrow ll\nu$, $WW \rightarrow l\nu l\nu$, Z +jets and W +jets. Figure 3.2 shows the observed E_T^{miss} distribution in the ee and $\mu\mu$ channels, compared to the signal and background predictions.

As discussed in Ref [22], an upper limit of 67% is placed on the Higgs \rightarrow DM branching ratio at the 95% confidence level. The dominant source of background is the $ZZ \rightarrow ll\nu\nu$ process, contributing $\approx 60\%$ of the background. $WZ \rightarrow ll\nu$ events, where the W boson decays into a electron or muon that escapes detection, account for 25% of the total background. $Z(\rightarrow ll)$ +jets process with misreconstructed E_T^{miss} contributes to about 8% of the total background, and non-resonant- ll processes, consisting of $t\bar{t}$, Wt , WW and $Z \rightarrow \tau\tau$ production contribute similarly. W +jets, VVV , and $t\bar{t}V(V)$ backgrounds contribute to a minor extent ($< 1\%$).

This thesis focuses on the ZZ background; its estimation and the uncertainty associated with it. In Ref [22], the ZZ background is estimated from simulation, with a total uncertainty of 10%.

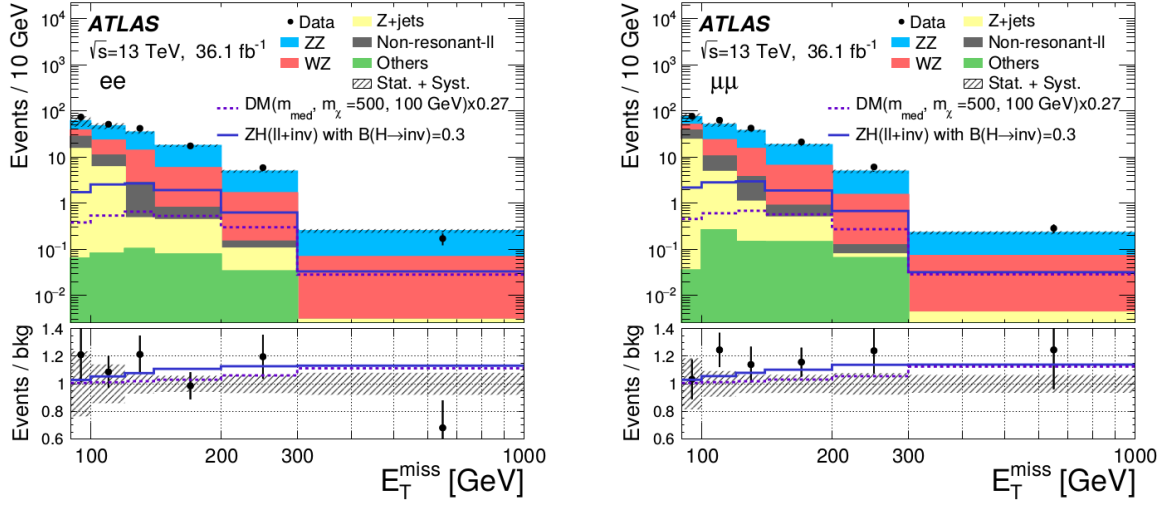


Figure 3.2: The observed E_T^{miss} distributions in the ee (left) and $\mu\mu$ channels, compared to the signal and background predictions. The total statistical and systematic uncertainty on the background predictions are shown by the error bands. The Standard Model background predictions are stacked. The $ZH \rightarrow ll + \text{invisible}$ signal distribution is shown with $B_{H \rightarrow \text{inv}} = 0.3$, and the simulated DM distribution is also scaled (with a factor of 0.27) to the best-fit contribution [22].

3.2 Background estimation: ZZ

It is difficult to identify $ZZ \rightarrow ll\nu\nu$ events, as their final state is identical to that of $ZH \rightarrow ll + E_T^{miss}$. Thus, the contribution of $ZZ \rightarrow ll\nu\nu$ is currently estimated using simulation. Figure 3.3 shows the Standard Model production of $q\bar{q} \rightarrow ZZ$ and $gg \rightarrow ZZ$. One of the Z bosons decays leptonically (into e^+e^- or $\mu^+\mu^-$), while the other Z boson decays into neutrinos ($\nu\bar{\nu}$). Neutrinos are very weakly interacting, and thus are invisible to the detectors at the LHC, and thus result in events with missing transverse momentum.

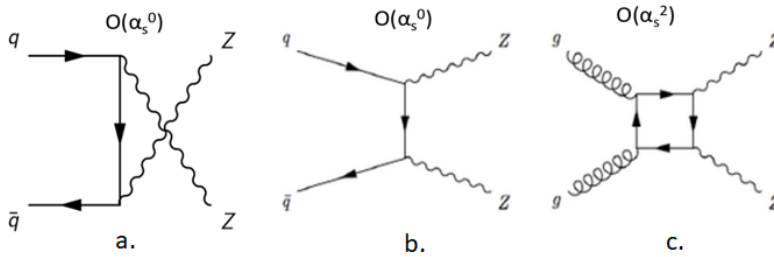


Figure 3.3: Feynman diagram showing ZZ production, in the s-channel (a) and t-channel (b) induced by $q\bar{q}$, and induced by gluons (c).

It is possible to estimate the $ZZ \rightarrow ll\nu\nu$ using $ZZ \rightarrow lll$ data. However, the precision of this process is statistically limited. The branching fraction $Z \rightarrow ll$ for one flavor of lepton (e/μ) is $\approx 3.4\%$, and $Z \rightarrow \nu\nu$ is 20%.

$$BR(ZZ \rightarrow lll) = (2 \times 0.034) \times (2 \times 0.034) = 0.00462 \quad (3.1)$$

$$BR(ZZ \rightarrow ll\nu\nu) = (2 \times 0.034) \times (0.2) \times 2 = 0.0272 \quad (3.2)$$

Thus, branching fraction of $ZZ \rightarrow lll$ ($\approx 0.46\%$) compared to $ZZ \rightarrow ll\nu\nu$ (2.7%), which is about 6 times higher. The low branching fraction of $ZZ \rightarrow lll$ limits the statistics.

Motivated by an analysis using γ +jets to estimate Z +jets [23], an alternative method to estimate $ZZ \rightarrow ll\nu\nu$ is to look at the $Z\gamma \rightarrow ll\gamma$ process. Figure 3.4 shows the leading order diagrams for the production of $Z\gamma$, where the Z boson further decays leptonically. Figures 3.4.a, b and c are similar to

the production of ZZ , with a photon instead of one of the Z bosons. The main differences in the two processes are the couplings of the photon and Z boson to the quarks, and the fact that photons are massless, whereas the Z boson is massive.

Figure 3.4.d gives the $ll\gamma$ final state, however, the photon is radiated off of a final state lepton, i.e. Final State Radiation (FSR). This process must be suppressed, which can be done by imposing a mass window on the reconstructed mass of the two leptons to be within 15 GeV of Z boson mass shell.

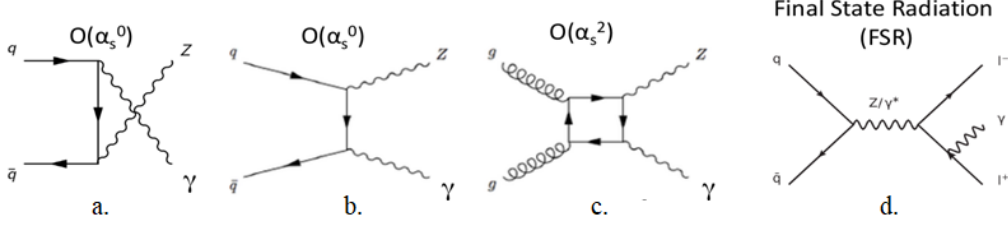


Figure 3.4: Feynman diagram showing $Z\gamma$ production, in the s-channel (a) and t-channel (b) induced by $q\bar{q}$, and induced by gluons (c). Diagram (d) shows a similar final state, but the photon is radiated off of a final state lepton (Final State Radiation).

At high Z boson transverse momentum, the $Z\gamma \rightarrow ll\gamma$ process should be kinematically similar to $ZZ \rightarrow ll\nu\nu$, as the mass of the Z boson will be negligibly small compared to its p_T . The $Z\gamma \rightarrow ll\gamma$ signal is also pure, and has a $\text{BR} \times \sigma$ as compared to $ZZ \rightarrow ll\nu\nu$. Thus, it should be possible to use $Z\gamma \rightarrow ll\gamma$ data to estimate the contribution of $ZZ \rightarrow ll\nu\nu$ in regions of high Z boson p_T .

3.3 Transfer factor R

To estimate the background, a transfer factor $R(p_T)$ is introduced, defined to be the ratio of the cross sections of $ZZ \rightarrow ll\nu\nu$ to $Z\gamma \rightarrow ll\gamma$ as a function of the p_T .

$$R(p_T) = \frac{\sigma_{ZZ}(p_T)}{\sigma_{Z\gamma}(p_T)} \quad (3.3)$$

With the two processes being kinematically similar at high p_T , R depends on the coupling of the Z and γ to quarks. It would be expected to reach a constant value at high p_T that can be determined theoretically. In the following paragraph, an attempt is made to obtain a simple approximate calculation of R from the contribution of qq process.

The photon - quark and Z boson - quark couplings in the Standard Model are given by,

$$-ieQ_q\gamma^\mu \quad \text{and} \quad \frac{-ie}{2\sin\theta_W\cos\theta_W}\gamma^\mu(v_q - a_q\gamma_5) \quad (3.4)$$

respectively, where Q_q , v_q and a_q are respectively the electric, vector and axial neutral weak couplings of the quarks, and θ_W is the weak mixing angle. There is a contribution due to the Z mass which appears in the internal propagators and phase space integration. This contribution becomes less important in the $p_T(\gamma) \gg M_Z$ region.

Thus, the leading order contributions from $q\bar{q} \rightarrow ZZ$ and $q\bar{q} \rightarrow Z\gamma$ are shown in Equation 3.5.

$$\begin{aligned} \sigma(q\bar{q} \rightarrow ZZ) &\propto \frac{1}{2} \frac{e^4 \{(v_q^2 + a_q^2)^2 + 4v_q^2 a_q^2\}}{16\sin^4\theta_W \cos^4\theta_W} \\ \sigma(q\bar{q} \rightarrow Z\gamma) &\propto \frac{e^2 Q_q^2 (v_q^2 + a_q^2)}{4\sin^2\theta_W \cos\theta_W} \end{aligned} \quad (3.5)$$

The u and d quarks present in a pp collision have different coupling strengths to the Z boson as stated in Ref [24], their relative contributions are accounted for using Equation 3.6

$$R = \frac{\sigma(u\bar{u} \rightarrow ZZ)\langle u \rangle + \sigma(d\bar{d} \rightarrow ZZ)\langle d \rangle}{\sigma(u\bar{u} \rightarrow Z\gamma)\langle u \rangle + \sigma(d\bar{d} \rightarrow Z\gamma)\langle d \rangle} \quad (3.6)$$

Using the vector and axial couplings of the Z boson to u and d quarks¹, assuming $\langle d \rangle / \langle u \rangle = 0.5$ and setting $\sin^2 \theta_W = 0.2315$, $R \approx 1.28$ for the dominant $q\bar{q}$ interaction. This approximate calculation has not been performed for gluon induced channels, as they involve loops and require a more involved calculation.

This transfer factor R may be used with $Z\gamma$ data to estimate the contribution of ZZ with reasonable accuracy at high p_T . To improve precision, it is necessary to estimate the theoretical uncertainties on the transfer factor R .

3.4 Theoretical Uncertainties

In this study, the following sources of theoretical uncertainties are studied.

- Missing higher order corrections: Contributions due to higher order QCD corrections cannot be calculated to arbitrarily high order, as it gets progressively more computationally expensive. Thus, this study is limited to Next to Leading Order (NLO), and further corrections are accounted for by varying the factorization and renormalization scales.
- Uncertainties associated with Parton Distribution Functions: A proton is a Baryon, and is composed of three valence quarks, and several gluons. Thus, proton-proton collisions, such as in the experiments conducted at the LHC, involve the interaction of these composite quarks and gluons (partons) at very high energies. These partons carry a fraction of the proton momentum. Parton Distribution Functions (PDFs) represent this fraction of proton momentum carried by partons as probability distributions. Owing to the non-deterministic nature of this fact, this study attempts to account for this uncertainties as PDF uncertainties.
- Photon Fragmentation Uncertainties: In the $Z\gamma \rightarrow ll\gamma$ process, the signal includes a photon. However, while reconstructing the event, soft photons, or photons resulting from other fragmentation processes may be encountered. To ensure that the photon is indeed prompt, it is required to be isolated from hadronic activity (such as pion decays). This isolation is implemented experimentally in different ways. The uncertainty associated with the implementation of this isolation is estimated as photon fragmentation uncertainties.

Each of these sources are explained further in their respective sections in Chapter 4.

3.5 Approach

Thus far, it has been established that a viable method to estimate the ZZ background contribution to the $ll+E_T^{miss}$ final state is to use $Z(\rightarrow ll)\gamma$ data, where the photon models the Standard Model invisible Z boson. A transfer factor R is introduced as the ratio of the cross sections of $ZZ \rightarrow ll\nu\nu$ to $Z\gamma \rightarrow ll\gamma$. In the high Z boson p_T region, the two processes are kinematically similar, therefore the curve of the transfer factor R as a function of p_T is expected to approach a constant value. This transfer can be used to estimate the contribution of $ZZ \rightarrow ll\nu\nu$ from $Z\gamma \rightarrow ll\gamma$ data.

This thesis estimates the theoretical uncertainties on the transfer factor. The $ZZ \rightarrow ll\nu\nu$ and $Z\gamma \rightarrow ll\gamma$ cross sections are obtained from MCFM, a femtobarn level matrix element generator. Varying the input parameters provided in the MCFM input file, the theoretical uncertainties are estimated.

¹Vector and Axial couplings of Z to u and d quarks: $v_u = 0.18, a_u = 0.50, v_d = -0.35, a_d = -0.514$

Chapter 4

Theoretical uncertainties on cross sections and the transfer factor R

4.1 MCFM

Monte Carlo for FeMtobarn processes (MCFM) is a program that calculates cross sections for femtobarn-level processes at leading order (LO) or next to leading order (NLO) QCD. In this study, MCFM v8.0 [25–28] is used to generate cross sections of $ZZ \rightarrow ll\nu\nu$ and $Z\gamma \rightarrow ll\gamma$ processes at NLO, with a selection of generator level cuts. The generation parameters in MCFM allow fine control over the sample, such as PDF sets, photon isolation, lepton and photon p_T and η , renormalization and factorization scales, etc. The samples are generated with cuts on $E_T^{miss} = p_T(Z \rightarrow \nu\nu)$ for the ZZ process and $p_T(\gamma)$ for the $Z + \gamma$ process. A ratio of these cross sections is taken to obtain the R distribution as a function of p_T . The uncertainty on R is calculated by varying several parameters at the generator level, such as the renormalization and factorization scales, the PDF sets used, photon fragmentation, etc. The contributions of the $q\bar{q}$ and gg processes are estimated separately.

In MCFM generated events containing a leptonically decaying Z boson, $Z \rightarrow ee$ only i.e. the decay is constrained to just one flavor, electrons. As electrons and muons have similar properties with the exception of mass, simply the branching fraction of $Z \rightarrow ee$ must be accounted for to obtain the inclusive value of R .

$$R_{inc} = R * \frac{BR(Z \rightarrow ee)}{BR(Z \rightarrow ee) * BR(Z \rightarrow \nu\nu) * 2} \quad (4.1)$$

Table 4.1 lists the generator level settings used for the ZZ and $Z + \gamma$ processes. All lepton cuts are consistent with the ones used in the ATLAS $Z + E_T^{miss}$ analysis [22].

Cuts	$ZZ \rightarrow ee\nu\nu$	$Z(\rightarrow ee) + \gamma$
Process ID	87	300
M_{ee}	$76 < M_{ee} < 106$ GeV	$76 < M_{ee} < 106$ GeV
$M_{\nu\nu}$	-	-
Order	NLO	NLO
PDF set	CT14	CT14
$p_T^{\text{lead}}(e)$	> 30 GeV	> 30 GeV
$ \eta^{\text{lead}}(e) $	< 2.47	< 2.47
$p_T^{\text{sublead}}(e)$	> 20 GeV	> 20 GeV
$ \eta^{\text{sublead}}(e) $	< 2.47	< 2.47
$p_T(V)^*$	> 90 GeV	> 90 GeV

Table 4.1: Settings in input.DAT for MCFM

The constraint on M_{ee} in the case of $Z + \gamma$ suppresses the FSR process by ensuring that the lepton pair

are from a Z decay only. In addition, the renormalization and factorization scales for both processes are set to be $H_T = \sum_i p_{T,i}$

4.2 Results

Using the settings listed in Table 4.1, the cross sections for $ZZ \rightarrow ee\nu\nu$ and $Z\gamma \rightarrow ee\gamma$ are generated, as shown in Figure 4.1. Throughout this analysis, these samples are the reference. The ratio $R =$

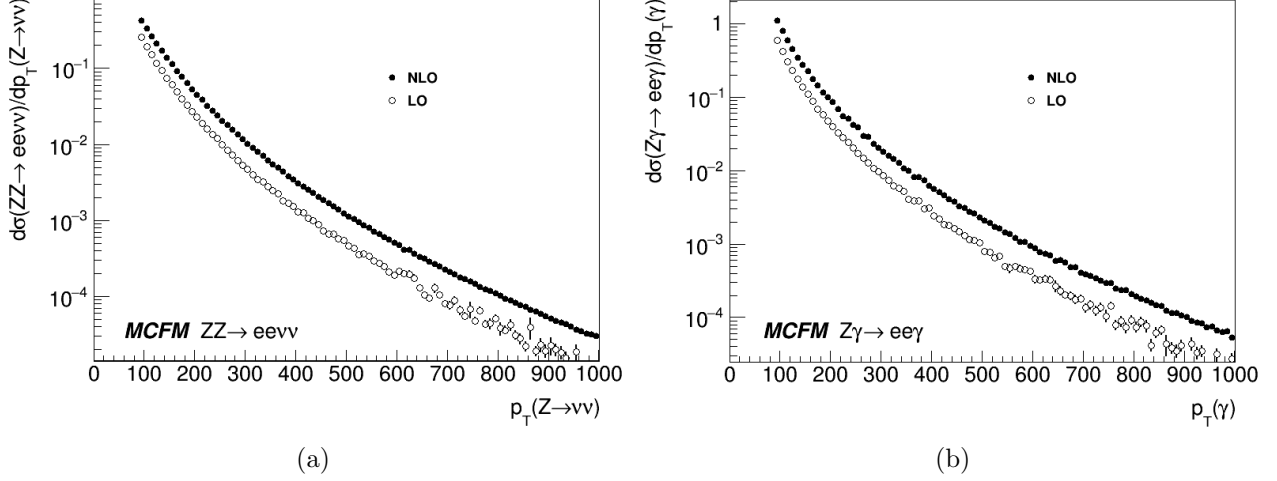


Figure 4.1: NLO and LO cross sections of $ZZ \rightarrow ee\nu\nu$ (left) and $Z\gamma \rightarrow ee\gamma$ (right) processes with the cuts as in Table 1. The vertical axis is in \log_{10} scale. The leptonically decaying Z boson decays to an e^+e^- pair. There is no flavor constraint on the neutrinos.

$\sigma(ZZ \rightarrow ee\nu\nu)/\sigma(Z\gamma \rightarrow ee\gamma)$ is shown in Figure 4.2, taken as the ratio of the cross sections in Figures 4.1a and 4.1b. Additional events are generated with E_T^{miss} and $p_T(\gamma) > 400$ GeV for the two processes respectively to increase statistics. The R value is observed to increase from ≈ 0.39 at 50 GeV to ≈ 0.52

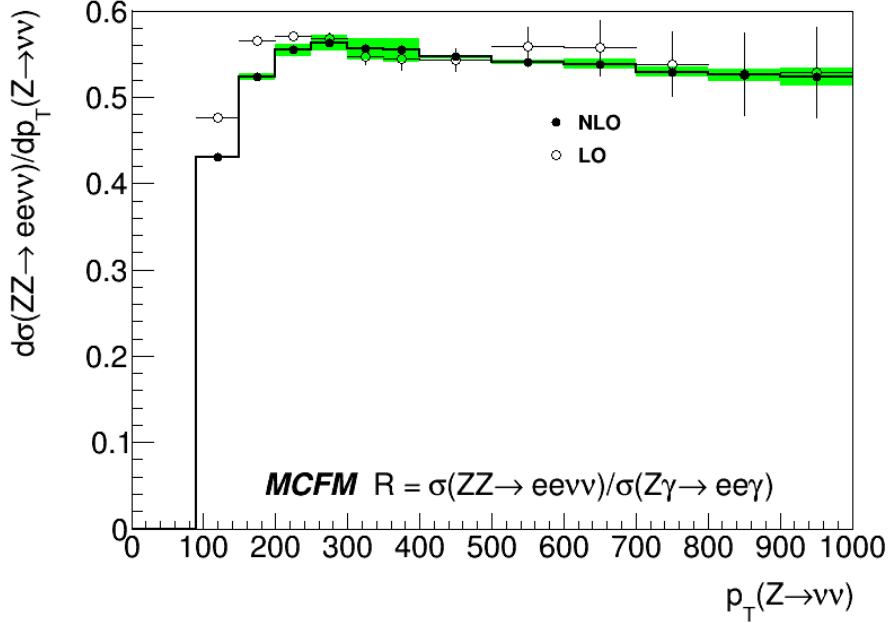


Figure 4.2: The transfer factor R as a function of p_T , taken as a ratio of the $ZZ \rightarrow ee\nu\nu$ and $Z\gamma \rightarrow ee\gamma$ cross sections at both LO and NLO. The leptonically decaying Z boson decays to an e^+e^- pair.

*V is a vector boson: $Z(\rightarrow \nu\nu)$ for the ZZ process; γ for the $Z\gamma$ process

at high p_T , where it reaches a plateau. When the branching ratio of Z boson decaying selectively to e^+e^- , or to $\nu\nu$, is accounted for as shown in Equation 4.1, the resulting ratio $R(p_T)$ is shown in Figure 4.3, which shows the ratio of $\sigma(ZZ)$ to $\sigma(Z\gamma)$, i.e. if the Z bosons do not decay further. The value of R is observed to increase from ≈ 0.98 at 50 GeV to ≈ 1.3 at high p_T , in reasonable agreement with the simple approximate calculation presented in Chapter 3 of $R \approx 1.28$.

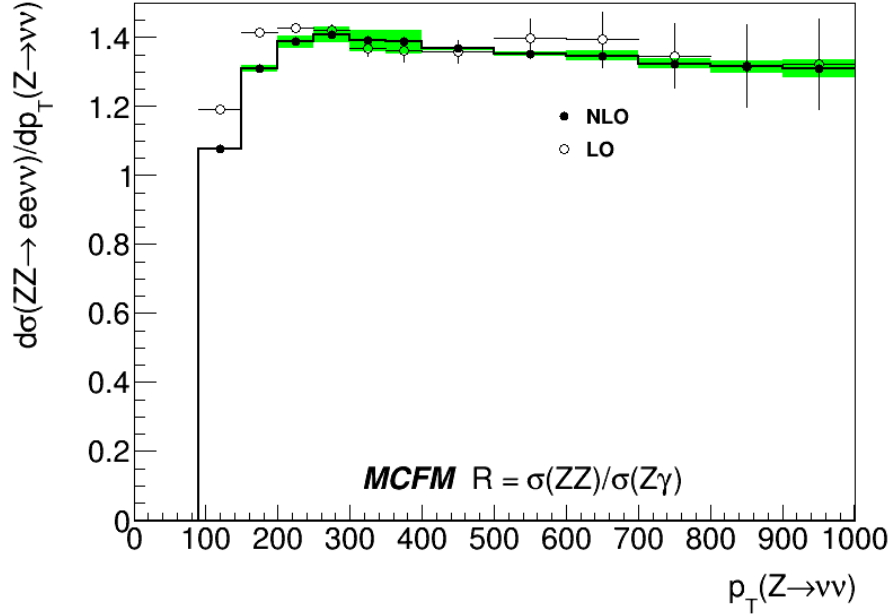


Figure 4.3: The transfer factor R as a function of p_T at both LO and NLO, adjusted for the $Z \rightarrow ee$ and $Z \rightarrow \nu\nu$ branching ratios. This shows the $R = \sigma(ZZ)/\sigma(Z\gamma)$, where the Z bosons do not decay.

Note : Need to flesh out the captions for the next few plots

Figure 4.4 shows the normalized rapidity distributions for missing transverse momentum ($Z \rightarrow \nu\nu$) and the photon respectively.

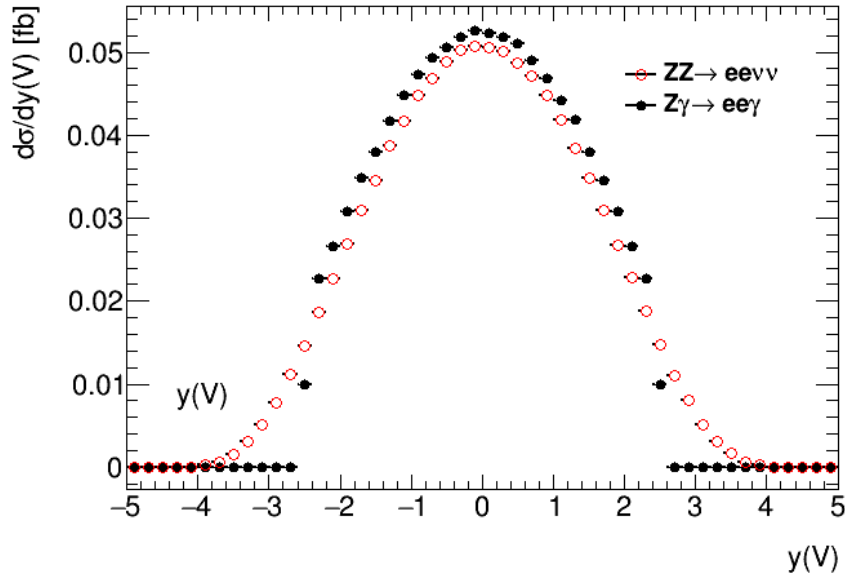


Figure 4.4: $y(V)$

Figures 4.5 and 4.6 further illustrate the topology of the events by showing normalized distributions for the leading and subleading lepton p_T and rapidity.

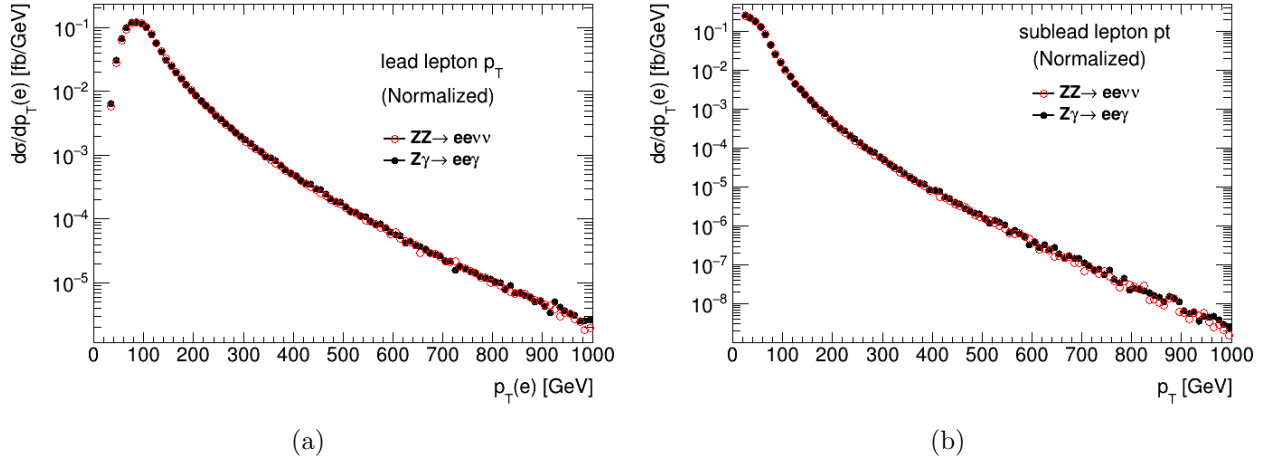


Figure 4.5: Normalized distributions showing the transverse momentum of the leading (left) and subleading (right) leptons for the two processes.

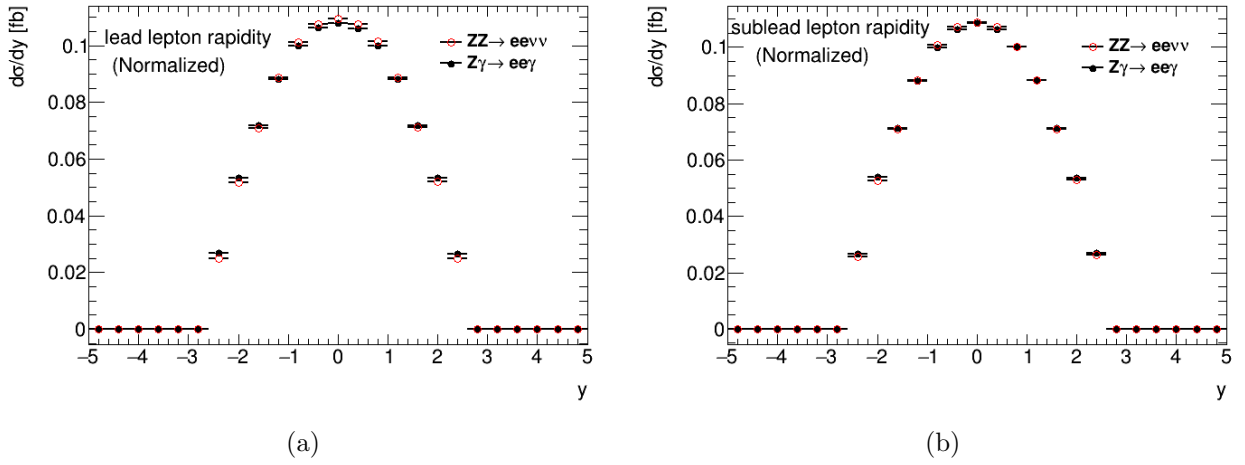


Figure 4.6: Normalized distributions showing the transverse momentum of the leading (left) and subleading (right) leptons for the two processes.

Gluon-gluon processes contribute to 8.6% of the total cross section for the ZZ process and 2.5% of the $Z + \gamma$ process. Figure 4.7 shows the ZZ and $Z\gamma$ cross sections (Z boson decay constrained to only e^-e^+ and $\nu\bar{\nu}$ only) from the contributing $q\bar{q}$, qg and gg subprocesses.

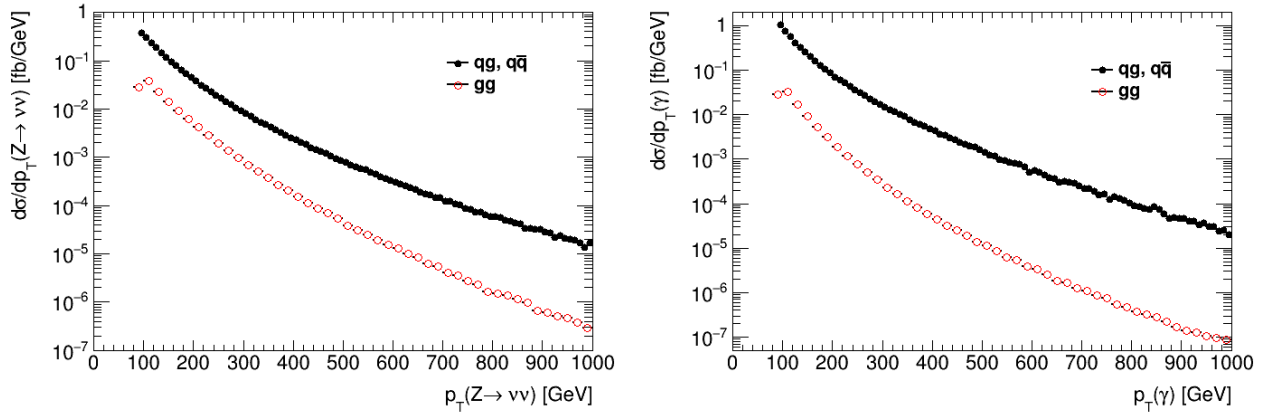


Figure 4.7: The cross sections of $ZZ \rightarrow ee\nu\nu$ (left) and $Z\gamma \rightarrow ee\gamma$ (right) as a function of p_T , from the contributing $q\bar{q}$, qg and gg processes. The leptonically decaying Z boson decays to an electron-positron pair

The R_{gg} distribution, shown in Figure 4.8 is observed to approach an asymptotic value at a much higher $p_T = 1.5$ TeV. The shape and scale of the R_{gg} distribution remain to be understood, as they differ from Figure 4.2.

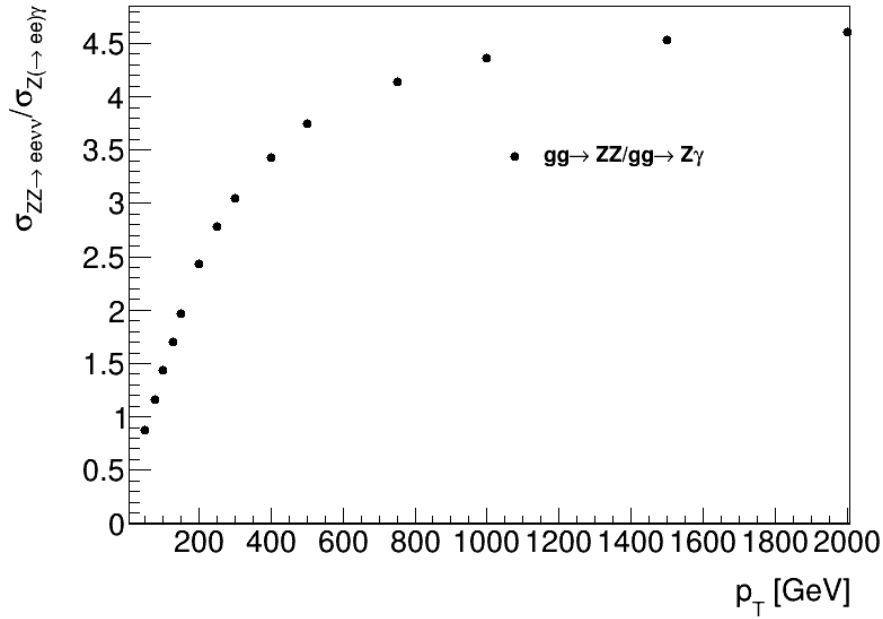


Figure 4.8: $R_{gg}(p_T)$, computed from the contributions of the gg subprocess to the cross sections of ZZ and $Z\gamma$. The curve reaches a plateau at a much higher p_T than for contributions from the $q\bar{q}$ process only.

4.2.1 Uncertainty from Scale Variation

In higher order QCD calculations, perturbative corrections may be added to the vertices or propagators in a Feynman diagram. Physically, these corrections occur at very small time scales. These loop integrals that correspond to these corrections diverge. The higher the order, the more difficult the calculation is. It is possible to introduce an arbitrary cut-off scale μ such that up to a given order, the effect of these corrections can be absorbed into the strong coupling constant $\alpha_s(\mu)$.

Two kinds of divergences are encountered: infrared divergences, and ultraviolet divergences. Infrared divergences occur for an on-shell internal propagator, and ultraviolet divergences are logarithmic divergences that occur as the integration variable approaches ∞ . They correspond to physics at long and short distances², respectively. The infrared divergences are addressed by the inclusion of the factorization scale μ_F , while the ultraviolet divergences are addressed by the inclusion of the renormalization scale μ_R . These parameters are arbitrary, and are set by hand. These are then varied between $\frac{1}{2}\mu < \mu < 2\mu$ to obtain an indication of the dependence of the matrix element on the scales, and thus, the uncertainty around the chosen scale.

To address scale uncertainties in this study, the prescription used in Ref [29], section 4 is followed. The central scale, μ_0 is chosen to be $H_T/2$ for both $ZZ \rightarrow ll\nu\nu$ and $Z\gamma \rightarrow ll\gamma$ samples (where H_T is the scalar sum of the transverse momentum of all particles after collision, $\sum_i p_{T,i}$), and seven-point variations are applied, i.e.

$$\frac{\mu_i}{\mu_0} = (1, 1), (1, 2), (2, 1), (2, 2), (0.5, 1), (1, 0.5), (0.5, 0.5) \quad (4.2)$$

where $i = 0, \dots, 6$. The central cross section value is taken to be the mean of the maximum and minimum cross sections resulting from this variation, and the uncertainty to be the half the difference

²Long distances are those where soft interactions take place, away from the hard parton-parton interaction. Short distances are those where the hard parton-parton interactions occur.

between the same.

$$\sigma_{NLO}^{(V)} = \frac{1}{2} \left[\sigma_{NLO}^{(V,max)} + \sigma_{NLO}^{(V,min)} \right] \quad (4.3)$$

$$\delta\sigma_{NLO}^{(V)} = \frac{1}{2} \left[\sigma_{NLO}^{(V,max)} - \sigma_{NLO}^{(V,min)} \right] \quad (4.4)$$

where

$$\sigma_{NLO}^{(V,max)} = \max \left\{ \sigma_{NLO}^{(V)}(p_T(V), \mu_i) | 0 \leq i \leq 6 \right\} \quad (4.5)$$

$$\sigma_{NLO}^{(V,min)} = \min \left\{ \sigma_{NLO}^{(V)}(p_T(V), \mu_i) | 0 \leq i \leq 6 \right\} \quad (4.6)$$

and $V = Z \rightarrow \nu\nu$ for $ZZ \rightarrow ll\nu\nu$, or $V = \gamma$ for $Z\gamma \rightarrow ll\gamma$. This uncertainty is propagated to R .

To estimate the degree of correlation between the processes, the process dependent part of the cross sections may be used. The highest available term in the perturbative expansion is considered to define a K -factor. Since the study is undertaken at NLO, the K -factor is defined as in Equation 4.7.

$$K_{NLO}^{(V)} = \sigma_{NLO}^{(V)}(p_T) / \sigma_{LO}^{(V)}(p_T) \quad (4.7)$$

To estimate the unknown process dependent correlation effects, the difference between the K -factors of the $ZZ \rightarrow ll\nu\nu$ and $Z\gamma \rightarrow ll\gamma$ processes is taken.

$$\delta^{(2)}\sigma_{NLO} = K_{NLO}^{(\gamma)}(p_T) - K_{NLO}^{(Z)}(p_T) \quad (4.8)$$

Applying the above prescription, the variation of scales for cross sections of $ZZ \rightarrow ee\nu\nu$ and $Z\gamma \rightarrow ee\gamma$ are shown in Figure 4.9 below.

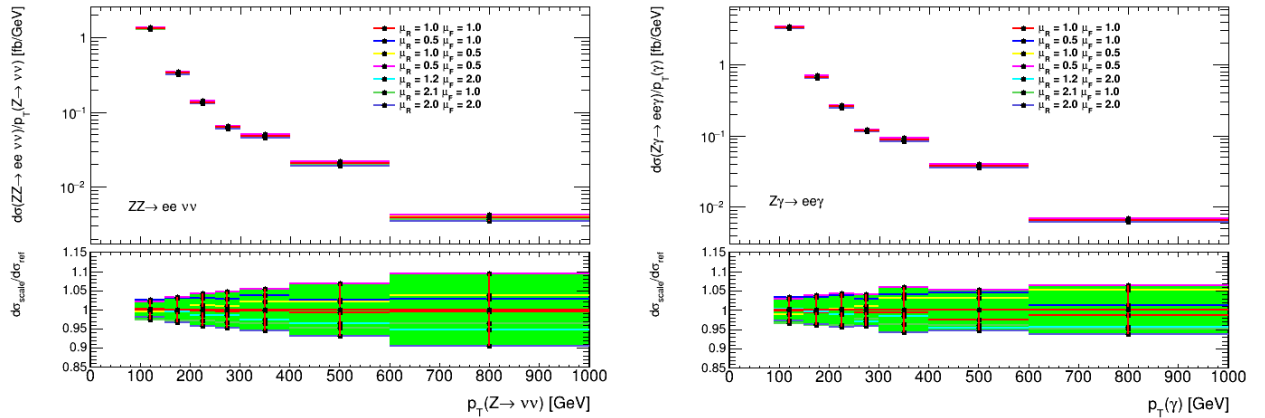


Figure 4.9: The scale variations around the cross sections of $ZZ \rightarrow ee\nu\nu$ (left) and $Z\gamma \rightarrow ee\gamma$ (right)

At 100 GeV, the deviation from the central value is about 3% for both processes and increases to 10% at high p_T . Here, the prescription in Equations 4.3 and 4.4 is used to compute the central value and uncertainty.

Treating the scales as correlated between the processes, the scale variation for the transfer factor R is shown in Figure 4.10. The central value of R and the uncertainty band around it is taken according to Equations 4.3 and 4.4 applied to R .

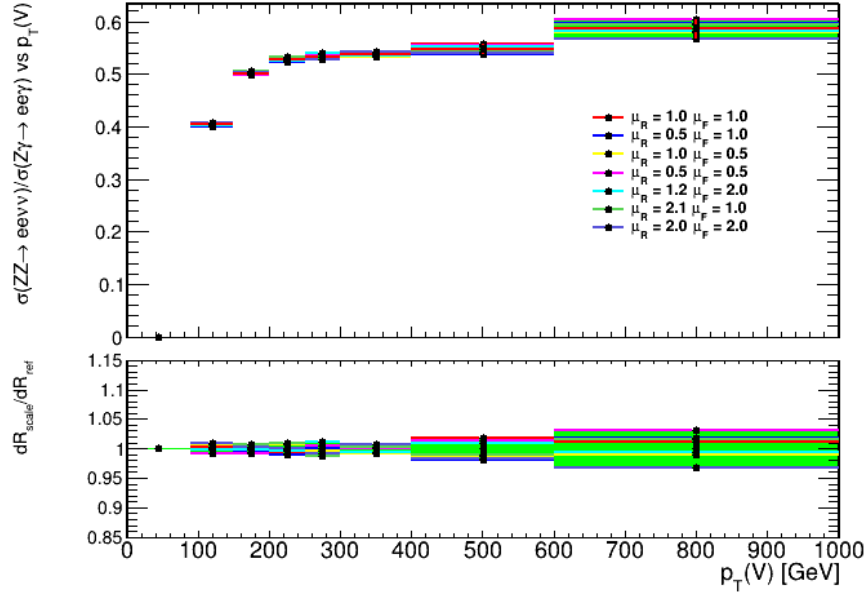


Figure 4.10: The transfer factor $R = \sigma(ZZ \rightarrow eev\nu)/\sigma(Z\gamma \rightarrow ee\gamma)$ (top), with the scales varied in a correlated manner for both ZZ and $Z\gamma$ processes. The bottom plot shows the relative ratio R_i/R_0 of the varied transfer factors to the central value.

The correlated scale uncertainty around R is lower compared to that of the individual cross sections. At 100 GeV, $R \approx 0.4 \pm 0.037$, or an uncertainty of 1%. At high p_T , $R \approx 0.55 \pm 0.01$, the uncertainty is 1.8%.

To study the uncertainty due to unknown process dependent correlation effects, the K -factor study is undertaken, following the prescription in Equations 4.7 and 4.8. Figure 4.11

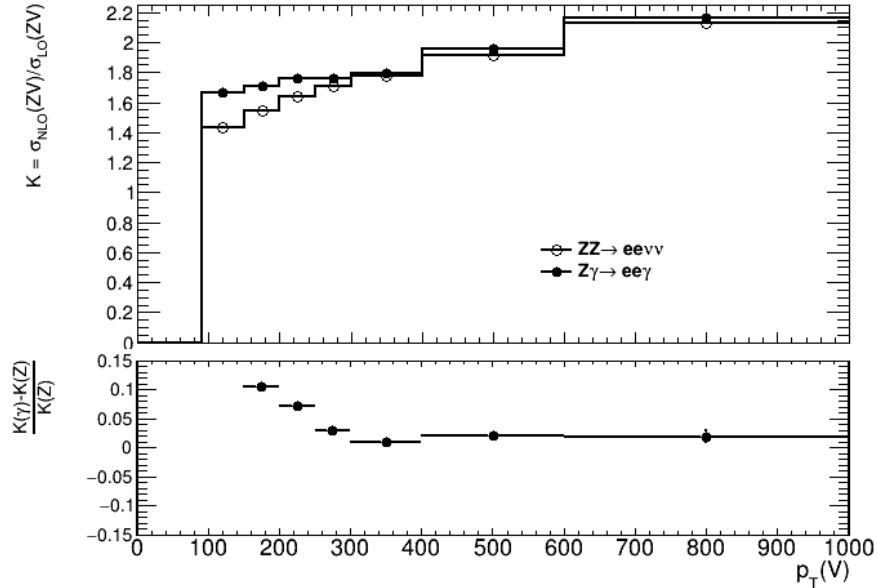


Figure 4.11: The K factor to estimate the unknown process dependent correlations, defined as $\sigma_{\text{NLO}}(V)/\sigma_{\text{LO}}(V)$. The bottom plot shows the K -factor difference relative to $K(Z)$.

Note : Work in progress with the last bin.

4.2.2 Uncertainty from PDF variation

A proton is a Baryon, i.e. it is composed of 3 quarks and several gluons. In a proton-proton collision, it is these quarks and gluons, called *partons* that actually interact. This is illustrated by Figures *the feynman diagrams in Chapter 3*, which show the Feynman diagrams for quark-quark and gluon-gluon interactions. Thus it is important to know the momentum of the interacting partons. It is not possible to deterministically know the momentum of the partons, as it is the momentum of the protons that is set during the experiment. However, the fraction of the proton momentum that is carried by the partons can be modelled as probability distributions.

Parton Distribution Functions (PDFs) characterize the fraction of proton momentum carried by partons as probability distributions. PDF sets are collections of PDFs that model the uncertainty associated with parton momenta. The PDF set used for reference is the CT14 [30] PDF set. The uncertainty on the PDFs is studied by using the 30 variations provided by the PDF4LHC15 set [31], constructed from the combination of CT14, MMHT14 [32] and NNPDF3.0 [33] PDF sets. These sets are provided by LHAPDF6 [34]. PDF4LHC15 provides a set of variations that include those determined by different groups (MSTW, CTEQ and NNPDF). The set used here is PDF4LHC15_nlo_30, consisting of 30 members. While the most accurate uncertainties are given by PDF4LHC15_nlo_100 set, PDF4LHC15_nlo_30 is used here for a faster, reasonably accurate estimate of the uncertainties.

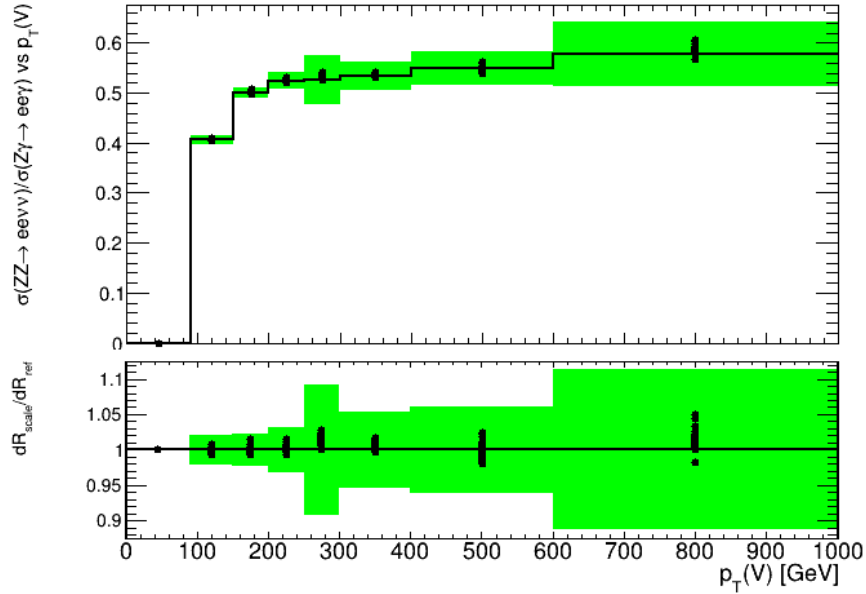


Figure 4.12: The transfer factor $R = \sigma(ZZ)/\sigma(Z\gamma)$ (top), and the relative ratio R_i/R_0 of the transfer factor calculated using PDF sets 1-30, with respect to set 0 which is taken as the central value.

Fig.4.12 shows the comparison of the ratio $R(p_T)$ from the 30 member sets of PDF4LHC15_nlo_30. To measure the uncertainty due to these 30 sets, analogous to Equation 20 in Ref [31], Equation 4.9 is used:

$$\delta^{PDF} R = \sqrt{\sum_{k=1}^{N_{mem}} (R^{(k)} - R^{(0)})^2} \quad (4.9)$$

where N_{mem} is the number of member sets in the group, in this case, 30.

Note : Still trying to figure out why the uncertainty is so large in the continuous distribution as opposed to the discrete data point run we did initially. Investigating statistical error by generating more high p_T events.

The combined uncertainty around $R \approx 0.40$ is ± 0.008 , or about 2%, at 100 GeV. The uncertainty is significantly larger at high p_T values, $> 10\%$.

4.2.3 Uncertainty from Photon Fragmentation

The $Z\gamma \rightarrow l\bar{l}\gamma$ process may contain photons that arise from the hadron showers. It is therefore important to isolate the prompt photon from hadronic activity. This reduces unwanted background from pion decays, or fragmentation processes.

Experimentally, photon isolation is implemented with the following cuts:

$$\sum_{\in R_0} E_T(\text{had}) < \epsilon_h p_T^\gamma \quad \text{or} \quad \sum_{\in R_0} E_T(\text{had}) < E_T^{\text{max}} \quad (4.10)$$

limiting the transverse hadronic energy $E_T(\text{had})$ in a cone of size $R_0 = \sqrt{\Delta\eta^2 + \Delta\phi^2}$ around the photon, to some fraction of the photon p_T , or some fixed small cut-off.

The smooth cone isolation method of Frixione [35] is an alternative isolation procedure, which simplifies calculations by avoiding fragmentation contributions. The following isolation prescription is applied to the photon:

$$\sum_{R_{j\gamma} \in R_0} E_T(\text{had}) < \epsilon_h p_T^\gamma \left(\frac{1 - \cos R_{j\gamma}}{1 - \cos R_0} \right)^n. \quad (4.11)$$

where $R_{j\gamma}$ is the separation of the photon and the j^{th} hadron. This requirement constrains the sum of hadronic energy inside a cone of radius $R_{j\gamma}$, for all separations $R_{j\gamma}$ less than a chosen cone size R_0 . This prescription allows soft radiation inside the photon cone, but collinear singularities are removed. The smooth cone isolation is infrared finite, thus fragmentation contributions do not need to be included.

The relative isolation, given by Equation 4.2.3 is used in experimental analyses, while smooth isolation is difficult to implement experimentally. However, comparing both methods gives us an estimate of the uncertainty due to the modelling of photon fragmentation.

In this analysis, R_0 is chosen to be 0.4 to agree with the experimental definition. The central value is chosen to be from the sample using smooth cone isolation (Frixione) with $\epsilon_h = 0.075$ and $n = 1$. These parameters are varied within a reasonable range to assess the uncertainty as shown in Figure 4.13.

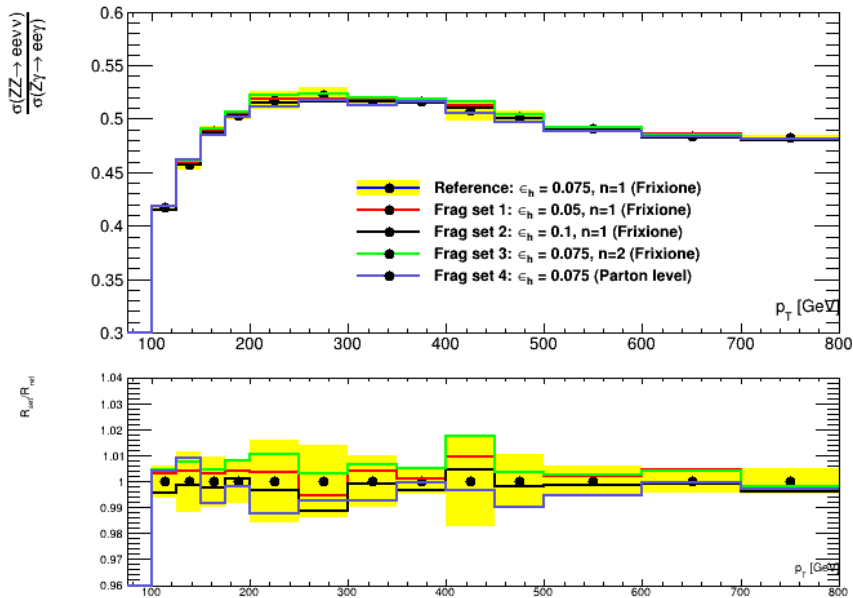


Figure 4.13: R distribution as a function of p_T , showing the uncertainty due to variation of photon isolation parameters ϵ_h and n in the smooth cone isolation procedure (Frixione), and ϵ_h in the photon isolation procedure. The lower panel shows the relative deviation of the varied sets from the central value, as well as the uncertainty band.

The uncertainty is calculated from the four sets listed in Figure 4.13:

$$\begin{aligned}\delta R_i &= |R_i - R_{ref}| & i \in (1, 2, 3, 4) \\ \delta R &= \sqrt{\max_{i=1,2,3} (\delta R_i)^2 + (\delta R_4)^2}\end{aligned}\tag{4.12}$$

as the effects assessed by changing the isolation definition in set 4, and varying the parameters in sets 1-3 are different.

The uncertainty is $< 2\%$ over the whole p_T range.

Chapter 5

Additional Figures

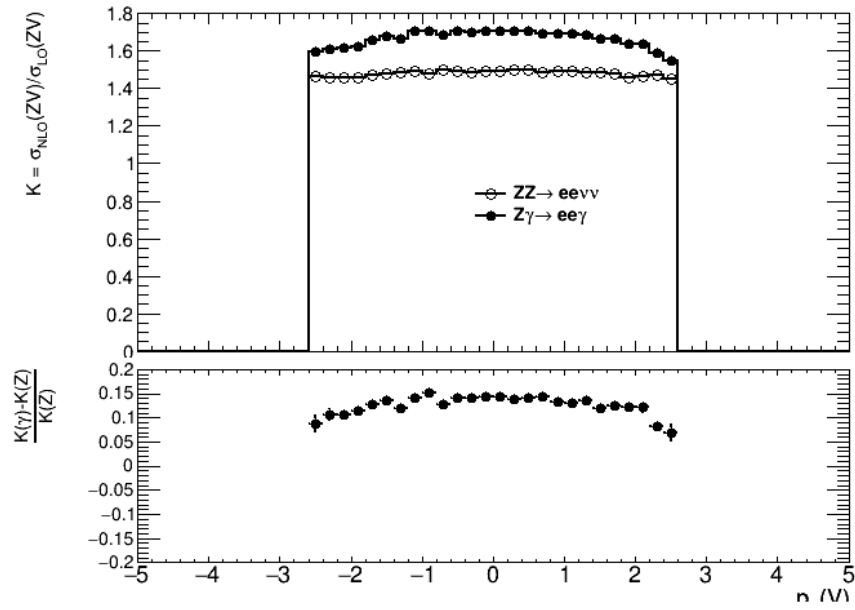


Figure 5.1: K factor as a function of rapidity

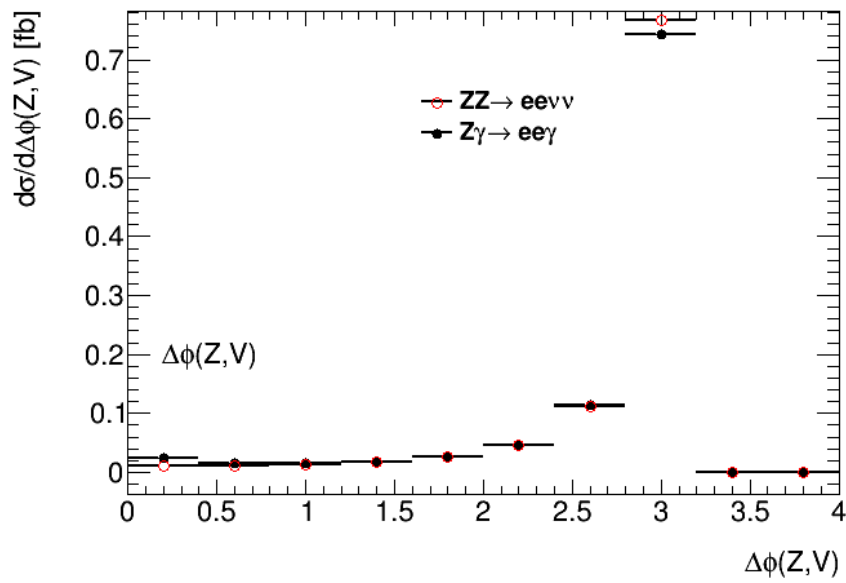


Figure 5.2: $d\phi(Z,V)$

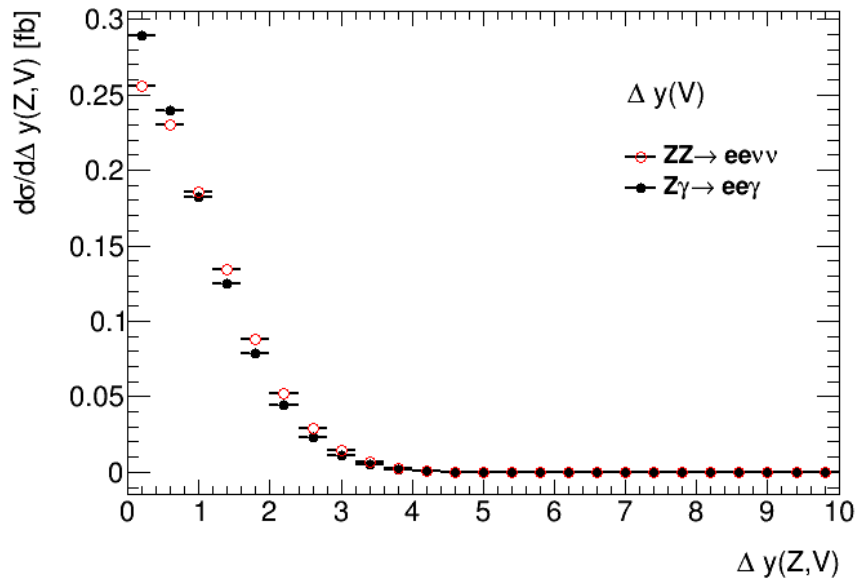


Figure 5.3: $d\sigma/d\Delta y(Z,V)$
Matter and Antimatter in the Universe

Bibliography

- [1] **D. J. Griffiths**, Introduction to Elementary Particles 2nd Edition, 2004 WILEY-VCH Verlag GmbH & Co. KGaA, Weinheim
- [2] PBS NOVA, Fermilab, Office of Science, United States Department of Energy, Particle Data Group.
- [3] **J. Greensite (2011)**. An introduction to the confinement problem. Springer. ISBN 978-3-642-14381-6.
- [4] **ATLAS Collaboration**, Observation of a New Particle in the Search for the Standard Model Higgs boson with the ATLAS detector at the LHC, Phys.Lett. B716 (2012) 1-29, [arXiv:1207.7214 \[hep-ex\]](#)
- [5] **A. O. Sushkov, W. J. Kim, D. A. R. Dalvit, S. K. Lamoreaux**, New experimental limits on non-Newtonian forces in the micrometer-range, Phys. Rev. Lett. 107, 171101 (2011), [arXiv:1108.2547 \[quant-ph\]](#)
- [6] **Jaco de Swart, Gianfranco Bertone, Jeroen van Dongen**, How Dark Matter came to matter, Nature Astronomy 1, 0059 (2017), [arXiv:1703.00013 \[astro-ph.CO\]](#)
- [7] **P. J. E. Peebles, Bharat Ratra**, The Cosmological Constant and Dark Energy (2002), [arXiv:astro-ph/0207347](#)
- [8] **Planck Collaboration**, Planck 2015 results. XIII. Cosmological parameters (2016), [arXiv:1502.01589 \[astro-ph.CO\]](#)
- [9] **N. Jarosik et al.**, Seven-Year Wilkinson Microwave Anisotropy Probe (WMAP) Observations: Sky Maps, Systematic Errors and Basic Results, Astrophys. J. Suppl. 192 14 (2011) [1001.4744], [arXiv:1001.4744 \[astro-ph.CO\]](#)
- [10] **M.C.Gonzalez-Garcia, Michele Maltoni**, Phenomenology with Massive Neutrinos, Phys.Rept.460:1-129,2008, [arXiv:0704.1800 \[hep-ph\]](#)
- [11] **Vernon Barger, Danny Marfatia, Kerry Lewis Whisnant**, The Physics of Neutrinos (2012), Princeton University Press, ISBN 0-691-12853-7
- [12] **Laurent Canetti, Marco Drewes, Mikhail Shaposhnikov**, Matter and Antimatter in the Universe, New J. Phys. 14 (2012) 095012, [arXiv:1204.4186 \[hep-ph\]](#)
- [13] **S. Weinberg**, Implications of Dynamical Symmetry Breaking, Phys. Rev. D13 (1976) 974–996, <https://doi.org/10.1103/PhysRevD.13.974>
- [14] **S. Weinberg**, Implications of Dynamical Symmetry Breaking: An Addendum, Phys. Rev. D19 (1979) 1277–1280, <https://doi.org/10.1103/PhysRevD.19.1277>
- [15] **L. Susskind**, Dynamics of spontaneous symmetry breaking in the Weinberg-Salam theory, Phys. Rev. D20 (1979) 2619–2625, <https://doi.org/10.1103/PhysRevD.20.2619>
- [16] **E. Gildener**, Gauge Symmetry Hierarchies, Phys. Rev. D14(1976) 1667, <https://doi.org/10.1103/PhysRevD.14.1667>

- [17] **Begeman, K. G., Broeils, A. H., Sanders, R. H.**, Extended rotation curves of spiral galaxies - Dark haloes and modified dynamics, Monthly Notices of the Royal Astronomical Society (ISSN 0035-8711), vol. 249, April 1, 1991, p. 523-537.
- [18] **Felix Kalhoefer**, Review of LHC Dark Matter searches, Int.J.Mod.Phys. A32 (2017) 1730006, arXiv:1702.0243 [hep-ph]
- [19] **Philip Harris, Valentin V. Khoze, Michael Spannowsky, Ciaran Williams**, Closing up on Dark Sectors at Colliders: from 14 to 100 TeV, Phys. Rev. D 93, 054030 (2016), arXiv:1509.02904 [hep-ph]
- [20] **Jing-Yuan, Edward W. Kolb, Lian-Tao Wang**, Dark matter coupling to electroweak gauge and Higgs bosons: an effective field theory approach, Phys.Dark Univ. 2 (2013) 200-218, arXiv:1305.0021 [hep-ph]
- [21] **ATLAS Collaboration**, Search for dark matter produced in association with a Higgs boson decaying to two bottom quarks in pp collisions at $\sqrt{s} = 8$ TeV with the ATLAS detector, Phys. Rev. D 93, 072007 (2016), arXiv:1510.06218 [hep-ex]
- [22] **ATLAS Collaboration**, Search for an invisibly decaying Higgs boson or dark matter candidates produced in association with a Z boson in pp collisions at $\sqrt{s} = 13$ TeV with the ATLAS detector, PLB 776 (2017), 318, arXiv:1708.09624 [hep-ex]
- [23] *Using $\gamma + jets$ to calibrate the Standard Model $Z(\rightarrow \nu\nu) + jets$ background to new processes at the LHC*
S. Ask, M. A. Parker, T. Sandoval, M. E. Shea, W. J. Stirling
Cavendish Laboratory, University of Cambridge, CB3 0HE, UK; 2011
[arXiv:1107.2803]
- [24] *2017 Review of Particle Physics - Particle Listings*
C. Patrignani et al. (Particle Data Group)
Chin. Phys. C, 40, 100001 (2016)
- [25] **J. Campbell, K. Ellis**, An update on vector boson pair production at hadron colliders, Phys. Rev. D 60 , 113006 (1999), arXiv:hep-ph/9905386
- [26] **J. M. Campbell, R. K. Ellis and C. Williams**, Vector boson pair production at the LHC, JHEP 1107, 018 (2011), arXiv:1105.0020 [hep-ph]
- [27] **J. M. Campbell, R. K. Ellis and W. Giele**, A Multi-threaded Version of MCFM, EPJ C75, 246 (2015), arXiv:1503.06182 [physics.comp-ph]
- [28] **John Campbell, Keith Ellis, Walter Giele, Ciaran Williams**, Monte Carlo for FeMtobarn processes (MCFM) v8.0 User Manual, <https://mcfm.fnal.gov/>
- [29] **J.M. Lindert, S. Pozzorini, et al.**, Precise predictions for $V + jets$ dark matter backgrounds, Eur. Phys. J. C (2017) 77: 829, arXiv:1705.04664 [hep-ph]
- [30] *New parton distribution functions from a global analysis of quantum chromodynamics*
Sayipjamal Dulat, Tie Jiun Hou, Jun Gao, Marco Guzzi, Joey Huston, P. Nadolsky, Jon Pumplin, Carl Schmidt, Daniel Stump, C. P. Yuan
arXiv:1506.07443
- [31] *PDF4LHC recommendations for LHC Run II*
[arXiv:1510.03865]
- [32] *Parton distributions in the LHC era: MMHT 2014 PDFs*
L. A. Harland-Lang, A. D. Martin, P. Motylinski, R. S. Thorne
arXiv:1412.3989

- [33] *Parton distributions for the LHC Run II*
The NNPDF Collaboration: Richard D. Ball, Valerio Bertone, Stefano Carrazza, Christopher S. Deans, Luigi Del Debbio, Stefano Forte, Alberto Guffanti, Nathan P. Hartland, Jose I. Latorre, Juan Rojo, Maria Ubiali
arXiv:1410.8849
- [34] *LHAPDF6: parton density access in the LHC precision era*
Andy Buckley, James Ferrando, Stephen Lloyd, Karl Nordstrom, Ben Page, Martin Ruefenacht, Marek Schoenherr, Graeme Watt
arXiv:1412.7420
- [35] *Isolated photons in perturbative QCD*
S. Frixione
Phys. Lett.B429(1998)369–374, hep-ph/9801442